Supporting Information

Restructuring-Resistant BiCuOS Superlattice Stabilizing Bi-O Coordination for Highly Selective CO_2 Electroreduction to Formate

Ganwen Chen[a,b#], Jie Chen[c,d#], Yukun Xiao[b], Meng Wang[b], Yishui Ding[b], Chenrui Ji[b], Lei Fan[b], Bailin Tian[b], Changjin Guo[b], Hexing Li[e], Yuecheng Xiong[b*], Zhangliu Tian[b,f*] and Wei Chen[b,c*]

[a] Joint School of National University of Singapore and Tianjin University, International Campus of Tianjin University, Binhai New City, Fuzhou 350207, PR China

[b] Department of Chemistry, National University of Singapore, 3 Science Drive 3, 117543, Singapore

[c] Department of Physics, National University of Singapore, 2 Science Drive 3, 117542,

[d] State Key Laboratory of Metal Organic Chemistry, Shanghai Institute of Organic Chemistry, Chinese Academy of Sciences, Shanghai, 200032, China

[e] The Education Ministry Key Lab of Resource Chemistry, Joint International Research Laboratory of Resource Chemistry of Ministry of Education, Shanghai Key Laboratory of Rare Earth Functional Materials, and Shanghai Frontiers Science Center of Biomimetic Catalysis, Shanghai Normal University, Shanghai 200234, China

[f] CAS Key Laboratory of Materials for Energy Conversion, Shanghai Institute of Ceramics, Chinese Academy of Sciences, Shanghai, 200050, PR China

[*] Corresponding Author E-mail: xiongyc@nus.edu.sg; tianzhangliu@mail.sic.ac.cn; phycw@nus.edu.sg (Wei CHEN)

Table of Contents

Supplemental Tables

Experimental Section

Synthesis of BiCuOS Ns. Solid-state reactions have been widely employed for the synthesis of oxychalcogenide compositions. Typically, the preparation methods for solid-state reactions are similar across different studies. In these methods, high-purity chemical powders with stoichiometric weights are thoroughly mixed and subsequently sealed within a vacuum quartz tube to create the desired samples. In this work, BiCuOS was prepared from the direct solid state reaction method between Bi_2O_3, Cu_2S, and Bi_2S_3. The feed ratio of these precursors was in a molar ratio of 2:3:1 and these precursors were carefully mixed, sealed in closed quartz ampoule in vacuum. Then the quartz ampoule was put in muffle furnace and calcined. Firstly, the sample was heated at a rate of 5℃ min^{-1} until reaching 573k and held for 30 minutes. Subsequently, the temperature was increased at a rate of 2℃ min^{-1} to 793k and maintained for 10 h. Finally, the sample was cooled at a rate of 5℃ min^{-1} until reaching room temperature. After calcining and cooling process, the sample was thoroughly ground and then stirred in a 1M hydrochloric acid solution for two hours to remove unreacted precursors, especially Bi_2O_3. The resulting product was washed three times through alternate centrifugation with ethanol and water to obtain the final product. The obtained product was granted into smaller particles (**Figure S2c**) for better distribution performance in ink.

Characterizations. The characterizations of the synthesized BiCuOS catalysts were examined by XPS with an Al/Mg twin X-ray source (Omicron DAR400) X-ray as the excitation source. Raman measurement system with 532 nm laser excitation and SpectraPro HRS-500 (Princeton Instruments) as detector was employed for Raman spectroscopy. Hard X-ray synchrotron radiation experiments were conducted at the hard X-ray branch of the Energy Materials Beamline (E-line, BL20U) at the Shanghai Synchrotron Radiation Facility (SSRF). Bruker D2 phaser powder X-ray analyzer equipped with Cu Kα radiation provided a measurement for XRD. The morphologies of the BiCuOS catalyst were examined by using a JEOL JSM-6701F SEM and JEM-2010 TEM. Gaseous products were analyzed using an online GC (Shimadzu 2014C).

Liquid products were identified by a ^{1}H-NMR spectrum (Bruker AVNEO 500 MHz system). The ATR-SEIRAS was obtained from Shimadzu spectrometers (IR tracer 100).

***Quasi-in-situ* XRD measurements.** Quasi-in-situ XRD experiments were performed using flow cells based on original electrocatalytic tests. After the corresponding activation time and different conditions, the electrolyte is immediately removed and XRD testing is performed.

***In-situ* Raman measurements.** In-situ Raman spectra experiments were performed using a top-plate cell photic apparatus linked to an electrocatalytic workstation. The experimental setup employed the same three-electrode configuration (working electrode (WE), reference electrode (RE), and counter electrode (CE)) and electrolyte solution as previously utilized in the electrocatalytic experiments. Before initiating Raman spectra measurements, CO_2 gas was infused into the electrolyte to ensure saturation. The *in-situ* Raman spectra were collected using a Renishaw InVia Qontor confocal Raman Microscope, which was equipped with a 532 nm laser excitation source.

***In-situ* ATR-SEIRAS measurement.** Prior to the spectrum test, the silicon (Si) prism specifically designed for *in-situ* ATR-SEIRAS measurements was cleaned and coated with a thin layer of Au film using a chemical deposition method described in the literature. After the deposition, the obtained Au film on the silicon prism was rinsed with deionized water and dried with air. The catalyst ink consisted of 9 mg of catalysts, 80 μL of 5 wt% Nafion, and 820 μL of isopropyl alcohol. The working electrode was prepared by depositing a total of 100 μL of the ink mixture onto the surface of the silicon prism. The working electrode was placed in a two-compartment with a three-electrode electrochemical cell. To avoid pollution from the counter electrode, the working electrode (catalyst on Si prism) and the reference electrode (Ag/AgCl in saturated KCl solution) were separated from a graphite rod as the counter electrode by an anion exchange membrane. The only stirring effect inside the cell was from various bubbled gases. The cell was integrated into a Fourier Transform Infrared Shimadzu spectrometer (IR Tracer 100) for the ATR-SEIRAS measurements. The electrochemical measurements were performed using a CHI 760E instrument. The experiments were carried out in a 0.5 M $KHCO_3$ solution as electrolyte at room temperature. Prior to the measurements, liquid nitrogen was added into the spectrometer. To ensure CO_2 saturation, a constant flow of CO_2 gas was purged into the electrolyte for 1 hour before *in situ* ATR-SEIRAS measurements, and the CO_2 flow was maintained throughout the electrochemical experiments. The spectra were presented in transmission mode, with negative peaks indicating an increase in the signal and positive peaks indicating a decrease in the signal. After finishing *in situ* ATR-SEIRAS measurements for each catalyst sample, the silicon prism was washed with an aqua regia solution to remove Au and the catalyst from its surface.

Electrochemical measurements. A CHI 760E electrochemistry working station (Shanghai CH Instruments) was employed for the electrochemical test. CHI 680C current booster (Shanghai CH Instruments) was combined with CHI 760E electrochemistry working station to achieve the measurement under high current density in CO_2R. The Ag/AgCl saturated KCl solution was used as the reference electrode, and the Ni foam was used as the counter electrode where the oxygen evolution reaction will happen. All potentials were calculated to the RHE with the following equation:

Equation 1

$$E_{RHE}=E_{Ag/AgCl}+0.197+0.059\times pH$$

And then compensated with necessary *iR*. During CO_2 reduction reaction measurements, 22 sccm of CO_2 was continuously fed to the gas chamber. The electrolyte (1 M KOH solution) was pumped to circulate through the catholyte and anolyte chambers pump. During the stability test, we addressed the flooding issue by applying a polytetrafluoroethylene solution (10%) spray onto the microporous layer of the carbon paper. This modification was implemented to improve the hydrophobicity of the GDE (Gas diffusion electrode).

To prepare the catalyst ink, we mixed 9 mg of catalysts with 80 μL of 5 wt % Nafion in 1 mL of isopropyl alcohol and deposited the mixture ink onto a carbon gas-diffusion layer on a 3 × 3 cm^2 carbon paper with an air spray gun. Next, we combined the diffusion-layer-coated catalyst with an anion exchange membrane and a nickel anode, using polytetrafluoroethylene spacers to create chambers between the anode and membrane, as well as the membrane and the cathode. Finally, we introduced a liquid electrolyte (1.0 M KOH) into these chambers. The area exposed to electrolyte and CO_2 gas was 1 cm^2. All catalysts were first pretreated for 30 minutes at current densities of 25 mA cm^{-2} before performing the eCO_2R performance tests.

Double-layer capacitance (C_{dl}). The electrochemically active surface area (ECSA) was estimated from the C_{dl} using cyclic voltammetry (CV) in a non-Faradaic potential region. The capacitive current density difference was determined as:

$$\Delta j = j_{\text{anodic}} - j_{\text{cathodic}}$$

where j_{anodic} and j_{cathodic} are the current densities obtained from the anodic and cathodic sweeps at the same potential, respectively. To isolate the capacitive component, we plotted (Δj/2) as a function of the scan rate (v). Because the capacitive current is proportional to v, the linear fit of (Δj/2) vs. v yields a slope equal to the C_{dl}.
Finally, the ECSA was estimated using:

$$\text{ECSA} = C_{dl}/C_s$$

where C_s is the specific capacitance of a smooth planar surface in the same electrolyte. Accordingly, the ESCA values of $BiCuOS^R$, $Bi_2O_3{}^R$, $Bi_2S_3{}^R$, and Bi_2O_3-Bi_2S_3-Cu_2S^R were calculated to be 14.95. 8.65, 8.8, and 9.93 according to the formula ESCA = Cdl/Cs (Cs = 40 μF cm^{-2}). Clearly, BiCuOS exhibited the largest ESCA.

Supplemental Figures

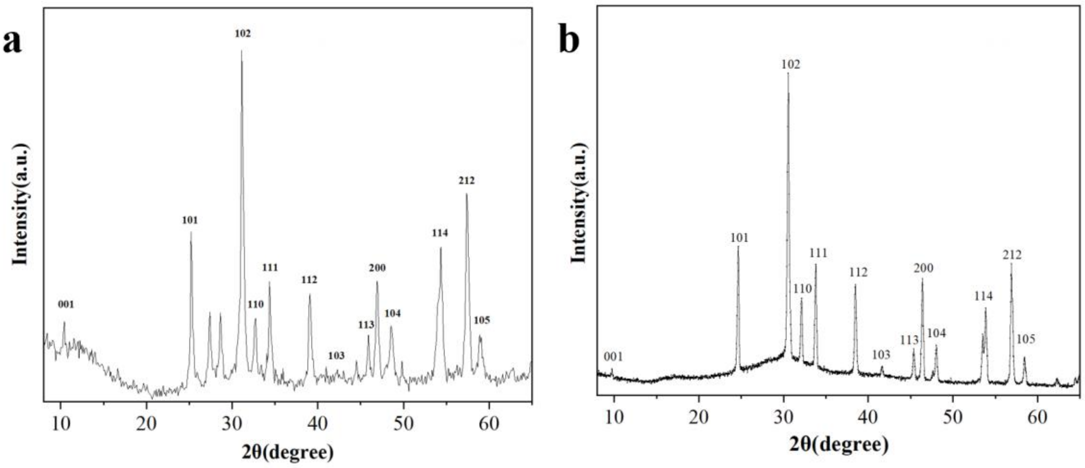

Figure S1 XRD pattern of the synthesized BiCuOS **(a)** before and **(b)** after acid wash. The synthesized sample was washed by 1M hydrochloride acid and then alternately washed with ethanol and deionized water.

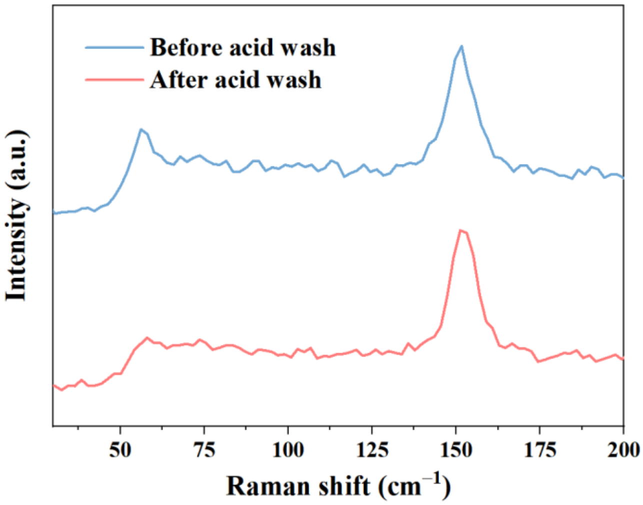

Figure S2 Raman Spectra of BiCuOS catalysts before and after acid wash.

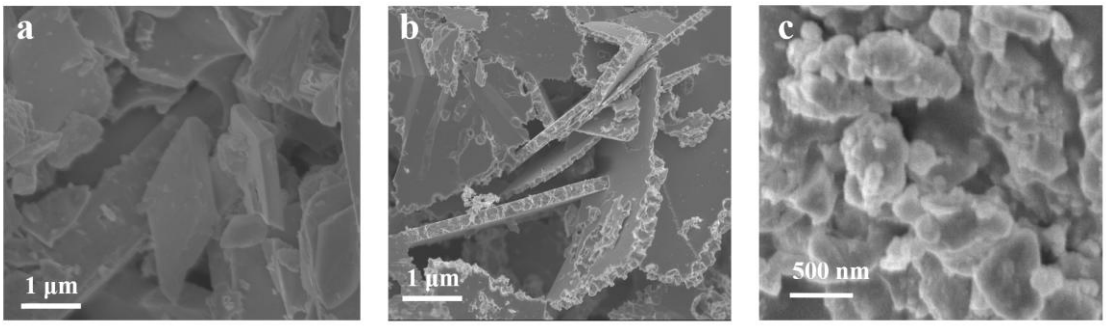

Figure S3 SEM images of BiCuOS **(a)** before, **(b)** after acid wash and **(c)** grinding.

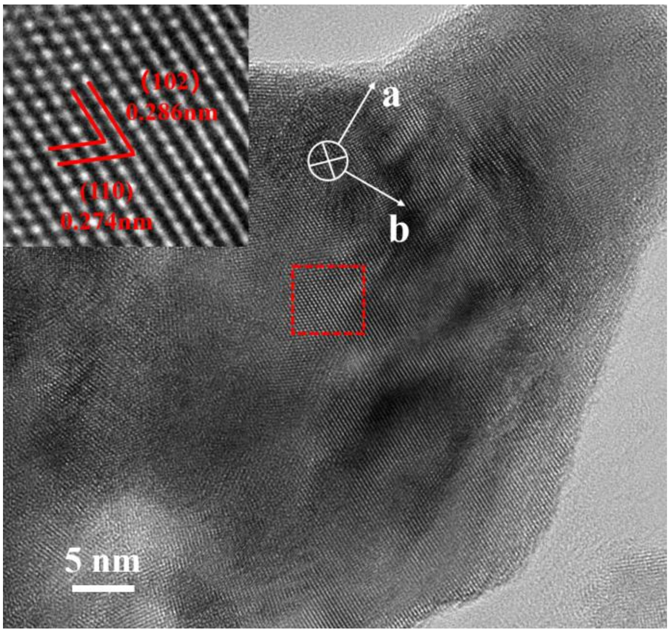

Figure S4 HRTEM image of the synthesized BiCuOS.

The careful inspection of the HRTEM image reveals local variations in the intensity of the atomic columns in the row of weak brightness located between two high-brightness zig-zag rows. Since the HRTEM image contrast is directly proportional to both thickness and atomic number (~Z^2), these contrasts can be directly interpreted using the structural model (**Fig. 1c**).

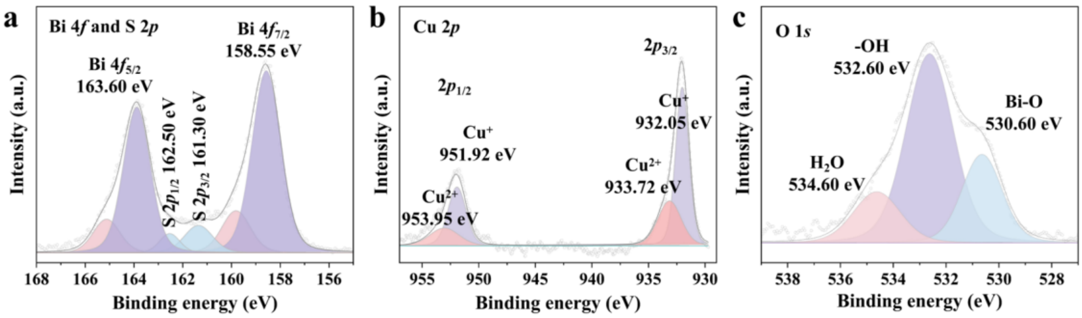

Figure S5 XPS spectra of **(a)** Bi 4*f* and S 2*p*, **(b)** Cu 2*p* and **(c)** O 1*s* of the BiCuOS before eCO_2R.

Dominant peaks in Bi 4*f* XPS spectra can be deconvoluted into four subpeaks at 158.55, 159.52, 163.60, 164.82 eV, respectively (**Fig. S4a**). Dominant peaks in Cu 2*p* XPS spectra can be deconvoluted into four subpeaks at 932.05, 933.72, 951.92, 953.95 eV, respectively (**Fig. S4b**). The O 1*s* XPS spectrum of pristine BiCuOS (**Fig. S4c**) can be split into three deconvolution peaks at approximately 530.60, 532.60, and 534.60 eV, which belong to Bi-O, Bi-OH, and surface-adsorbed oxygen species, respectively.

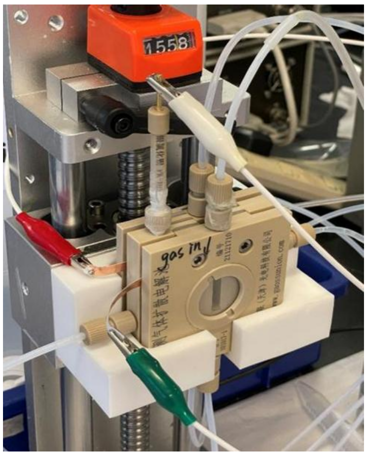

Figure S6 The photo of the three-electrode flow cell system. The working electrode (WE) consists of a catalyst-deposited gas diffusion layer with a working area of 1 cm^2. The reference electrode (RE) is an Ag/AgCl electrode, while the counter electrode (CE) is made of platinum (Pt). In the system, CO_2 gas is continuously supplied through a steady flow pump at a flow rate of 20 mL/min. The electrolyte is pumped into the anode and cathode cells using a peristaltic pump.

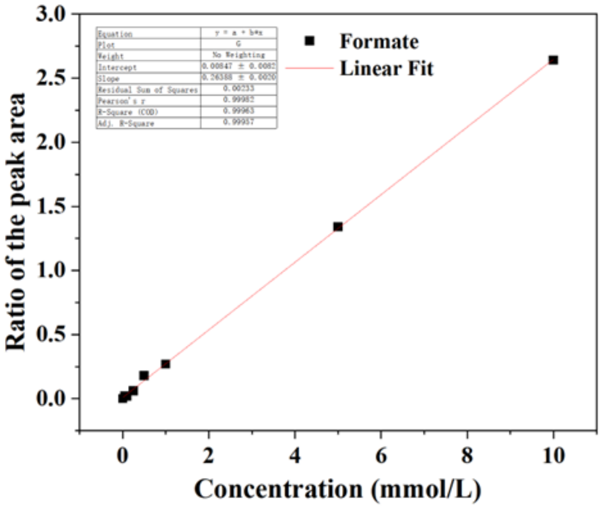

Figure S7. Internal standard substance slopes.

The R-square accuracy larger than 0.99 which represent that this is a successful Internal standard substance.

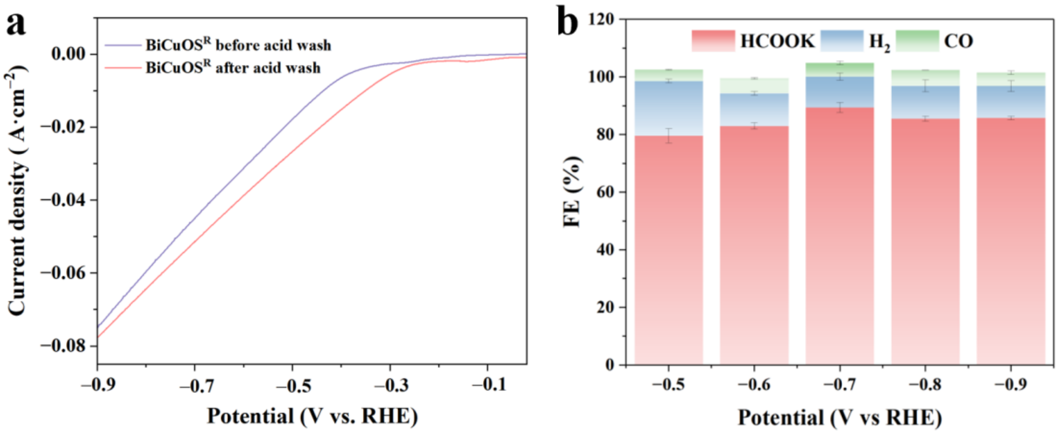

Figure S8 (a) LSV curves among BiCuOS^R before and after acid wash. (b) eCO$_2$R performance in 0.5 M KHCO$_3$ with iR compensation. FE of formate, CO and H$_2$ for synthesized BiCuOS NSs before acid wash.

To clarify the possible influence of the acid-washing step on the catalytic behavior of BiCuOS, we additionally compared the eCO$_2$R performance of the as-prepared sample before and after acid washing. As shown in **Fig. S8**, the acid-washed BiCuOS exhibits consistently higher formate selectivity than the unwashed sample over the potential range. These results indicate that the acid-washing treatment does not deteriorate the catalytic performance of BiCuOS. Instead, the improved selectivity after acid washing is more likely associated with the removal of residual unreacted precursor phases and the resulting improvement in phase purity, rather than substantial alteration of the intrinsic BiCuOS framework.

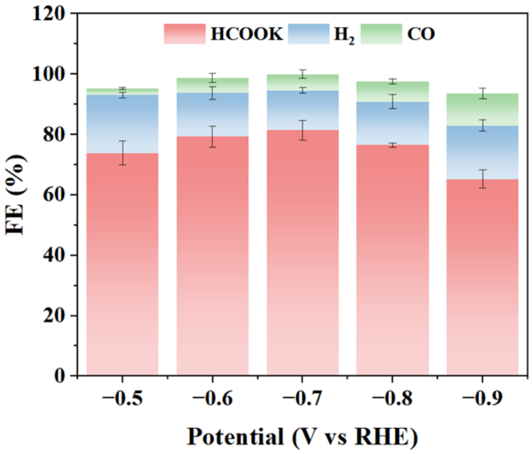

Figure S9 eCO_2R performance in 0.5 M $KHCO_3$ with iR compensation. FE of formate, CO and H_2 for Bi_2O_3 Ns. All data with error bars are based on three independent replicates.

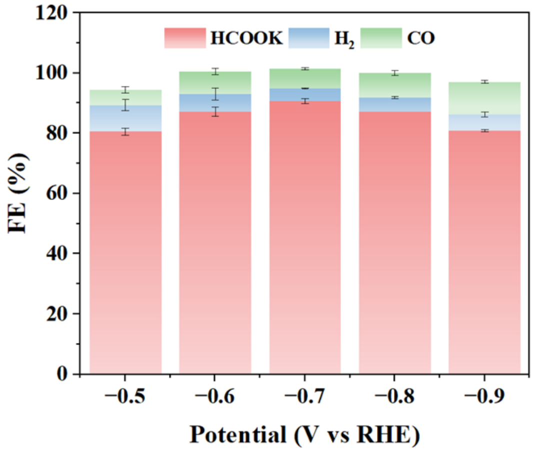

Figure S10 eCO_2R performance in 0.5 M $KHCO_3$ with iR compensation. FE of formate, CO and H_2 for Bi_2S_3 Ns. All data with error bars are based on three independent replicates.

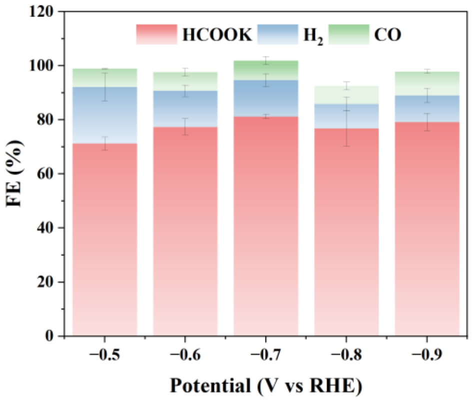

Figure S11 eCO_2R performance in 0.5 M $KHCO_3$ with iR compensation. FE of formate, CO and H_2 for Bi_2O_3-Bi_2S_3-Cu_2S heterojunction structure Ns. All data with error bars are based on three independent replicates.

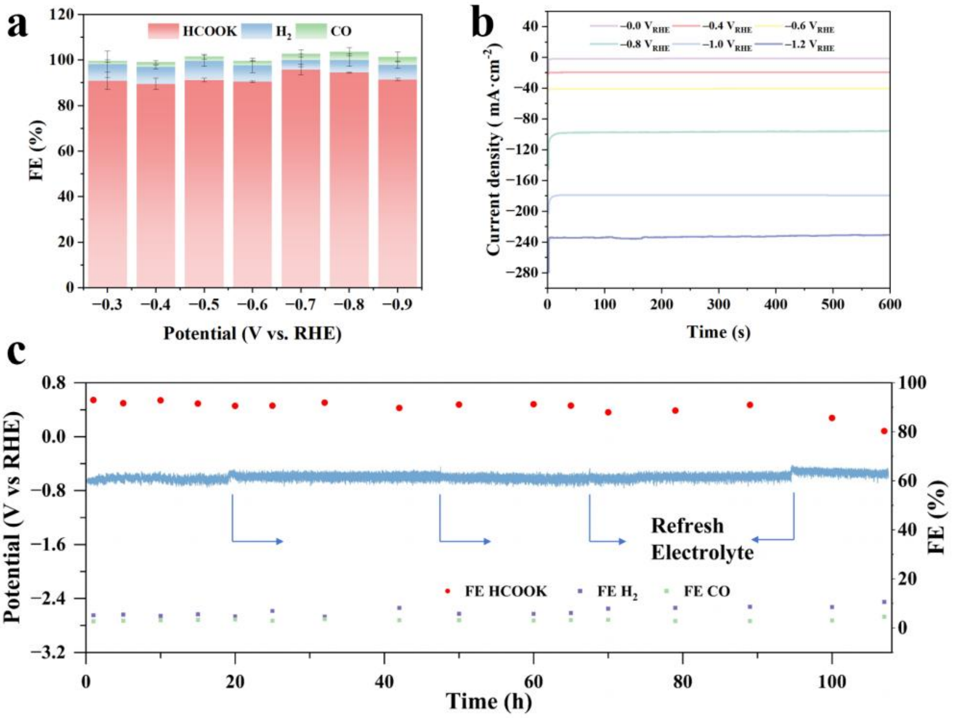

Figure S12 (a) eCO_2R performance in 1M KOH with iR compensation. FE of formate, CO and H_2 for BiCuOS Ns. **(b)** Chronoamperometric curves of BiCuOS at different potentials with iR compensation in 1 M KOH. **(c)** 107 h Chronoamperometry results for BiCuOS at –0.75 V_{RHE} with iR compensation in 1 M KOH.

Although excellent performance was achieved under neutral conditions, alkaline electrolytes are typically employed in practical eCO_2R systems due to their ability to suppress the competing HER and improve CO_2 utilization efficiency. Therefore, the catalytic performance of BiCuOS was further evaluated in 1 M KOH. The results showed that BiCuOS maintained excellent formate selectivity and high current density across a wide potential range. BiCuOS catalysts were further evaluated in 1 M KOH. The results showed that it maintained excellent formate selectivity and high current density. Across a wide potential range, the FE for formate consistently exceeded 90%, indicating that BiCuOS retains outstanding formate selectivity in alkaline electrolyte. The proportions of CO and H_2 byproducts were minimal, suggesting that side reactions were effectively suppressed (**Fig. S12a**). The chronoamperometric curve under constant potential exhibited stable current without significant decay, demonstrating the good electrochemical stability of BiCuOS in alkaline media (**Fig. S12b**). When operated at a constant current density of 50 mA cm^{-2} for 107 hours, the potential remained stable at –0.75 VRHE, and the FE for formate was maintained at 92% (**Fig. S12c**).

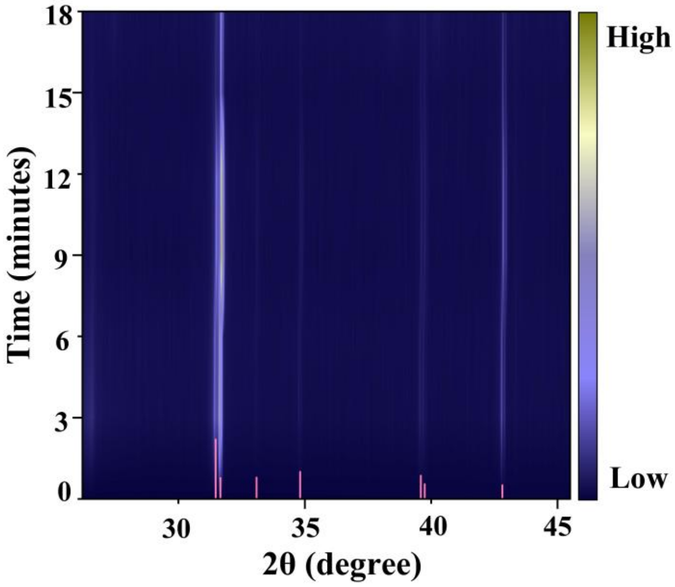

Figure S13 Time-resolved *quasi-in-situ* XRD heat map of BiCuOS nanosheets during eCO_2R in 0.5M $KHCO_3$ as electrolyte under current density of 20 mA cm^{-2}.

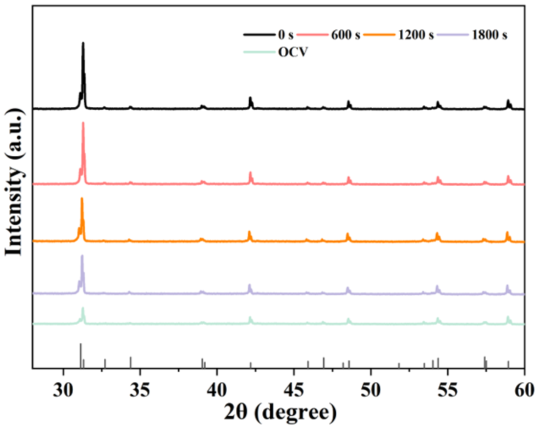

Figure S14 Time-resolved *quasi-in-situ* XRD patterns of BiCuOS nanosheets during eCO_2R in 1 M KOH as electrolyte under current density of 20 mA cm^{-2}.

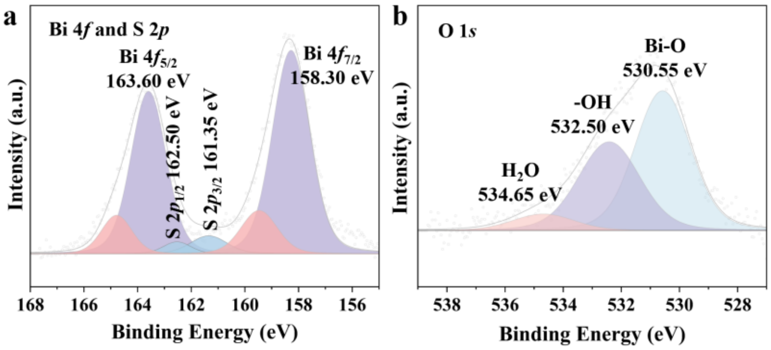

Figure S15 XPS spectra of **(a)** Bi 4*f* and S 2*p*, **(b)** O 1*s* of the BiCuOS after eCO_2R. The Bi 4*f* spectra shows no detectable changes in binding energy, indicating that the Bi oxidation state remains unchanged. The O 1*s* XPS spectrum of $BiCuOS^R$ can be deconvoluted into three deconvolution peaks. The peaks at 530.55, 532.50, and 534.65 eV corresponds to Bi–O, Bi–OH, and surface-adsorbed carbonate species, respectively. Notably, the Bi–O peak exhibits no shift, further confirming the preservation of Bi–O coordination of BiCuOS during eCO_2R.

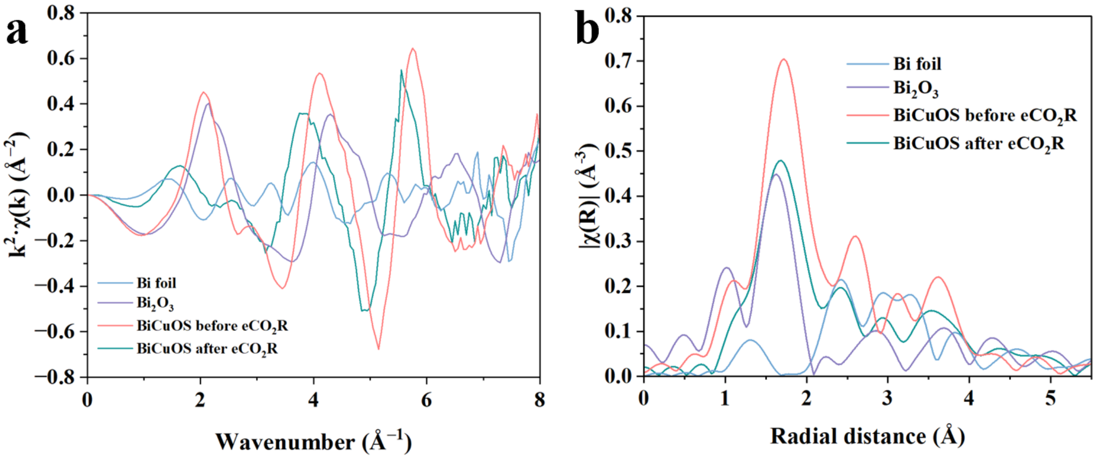

Figure S16 (a) q space curves of Bi L3-edge FT-EXAFS for BiCuOS, BiCuOS^R and reference samples. **(b)** The corresponding R-space radial distribution function diagram. The FT-EXAFS show that the dominant peak of BiCuOS^R appears at 1.7 Å, which is consistent with the pristine BiCuOS and can be assigned to the first shell Bi–O coordination. The slight attenuation of the peak intensity indicates minor surface perturbations, while confirming that the majority of Bi–O bonds remain intact after eCO$_2$R

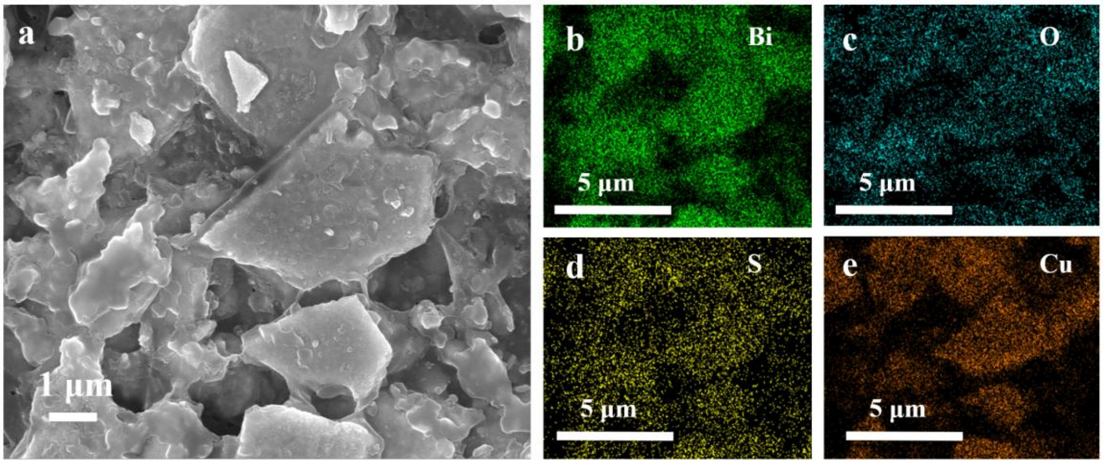

Figure S17 (a) SEM image of BiCuOS after stability test. **(b-e)** sem mapping images of each element of BiCuOS after stability test.

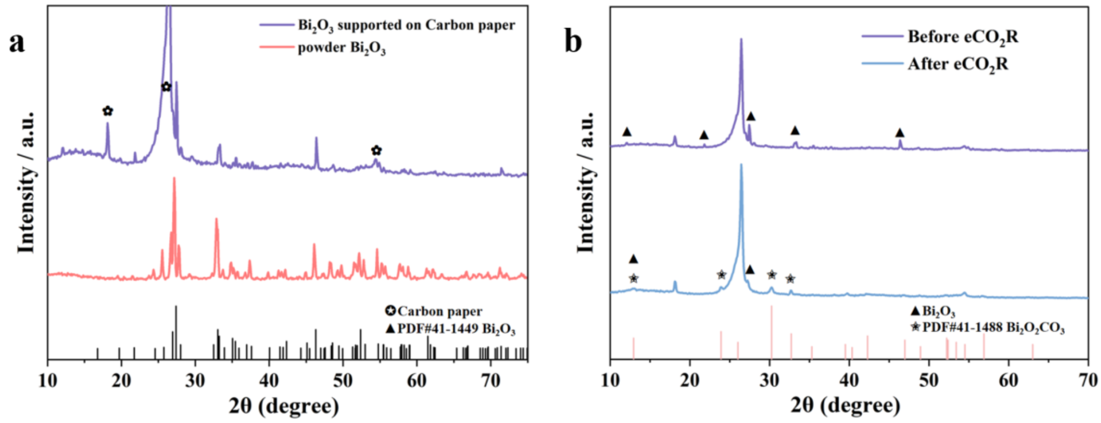

Figure S18 XRD patterns of Bi_2O_3 nanosheets **(a)** before, **(b)** after eCO_2R in 0.5 M $KHCO_3$.

After the reaction, bismuth oxide transforms into small-sized nanoparticles composed of a substantial amount of self-reduced metallic Bi along with bismuth oxycarbonate species (**Fig. S18-20**).

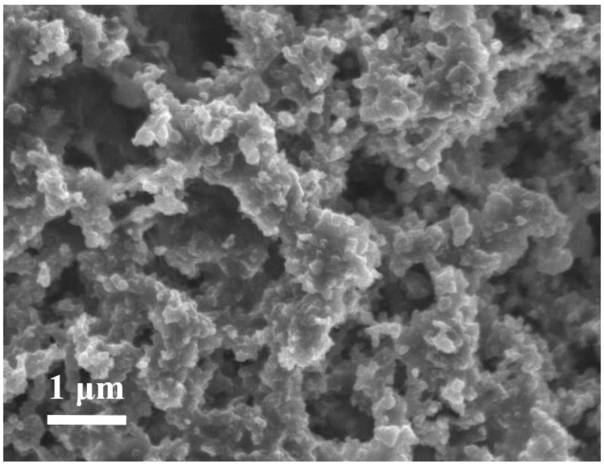

Figure S19 SEM image of Bi_2O_3 NSs after eCO_2R.

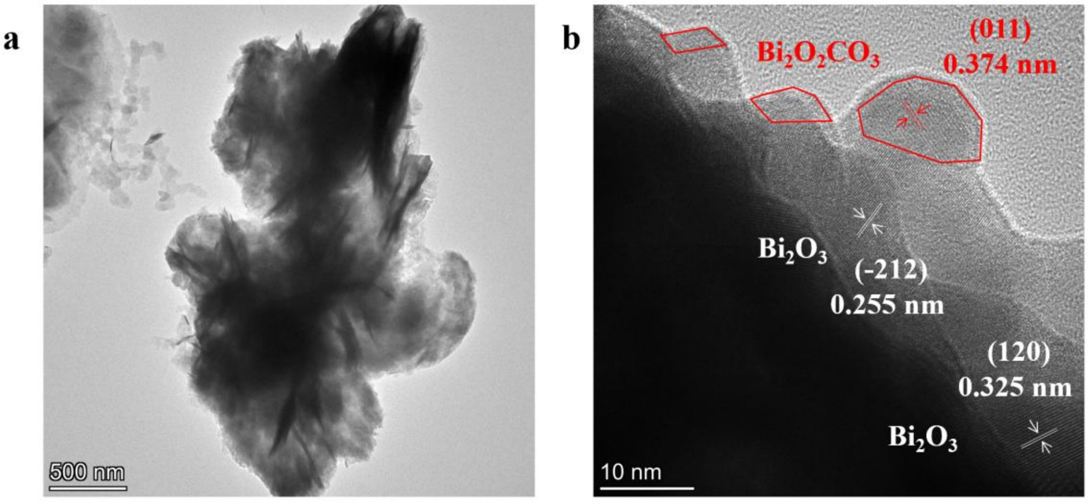

Figure S20 (a) TEM image, **(b)** HRTEM image of Bi_2O_3 NSs after eCO_2R.

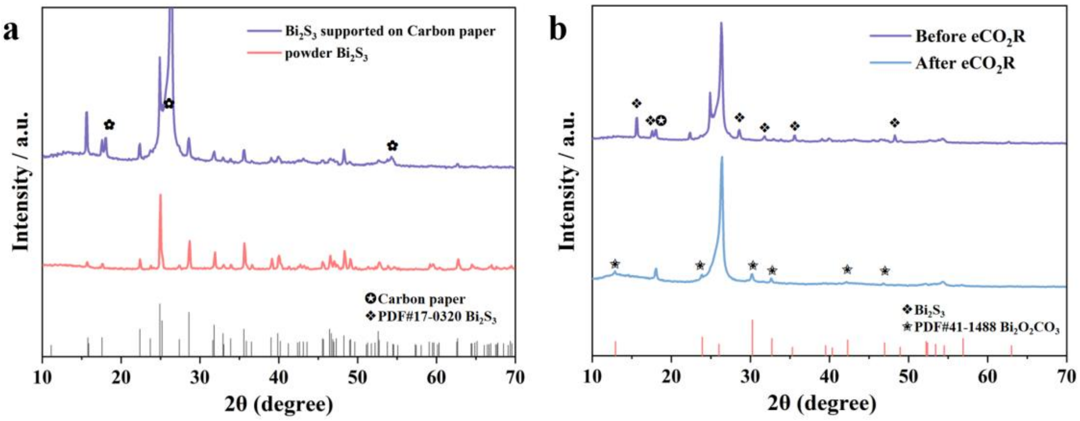

Figure S21 XRD patterns of Bi_2S_3 nanosheets **(a)** before, **(b)** after eCO_2R in 0.5 M $KHCO_3$.

In the case of bismuth sulfide undergoes significant morphological restructuring, evolving into a flower-like structure (**Fig. S22)**. In addition, XRD analysis and TEM reveal that the bismuth oxycarbonate is formed after the reaction (**Figure S21-S23)**.

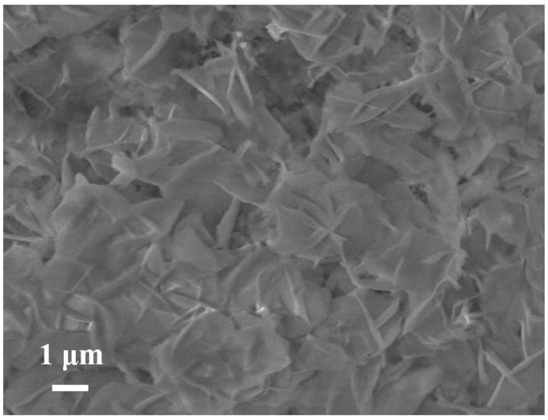

Figure S22 SEM image of Bi_2S_3 NSs after eCO_2R.

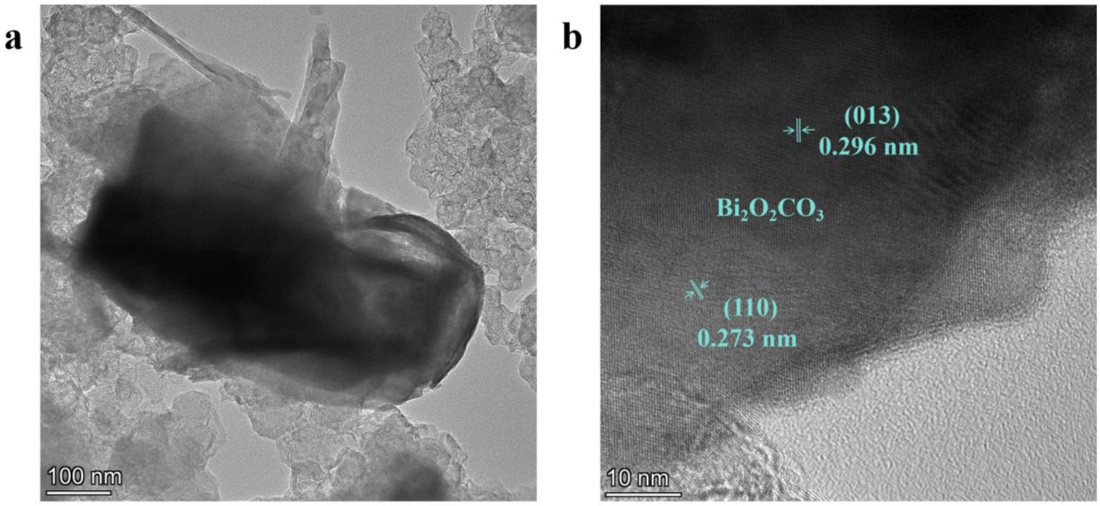

Figure S23 (a) TEM image, **(b)** HRTEM image of Bi_2S_3 NSs after eCO_2R.

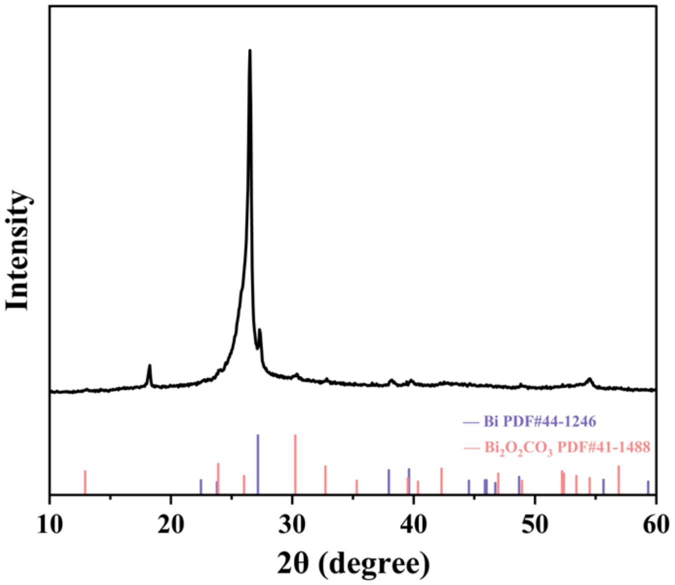

Figure S24 XRD patterns of Bi_2O_3-Bi_2S_3-Cu_2S NSs after eCO_2R in 0.5 M $KHCO_3$.

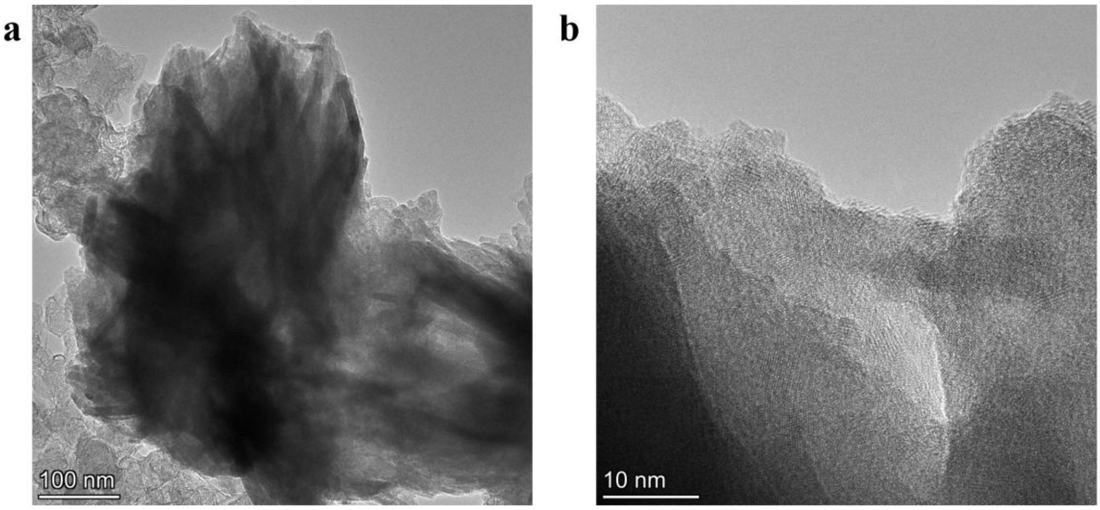

Figure S25 (a) TEM image, **(b)** HRTEM image of Bi_2O_3-Bi_2S_3-Cu_2S NSs after eCO_2R.

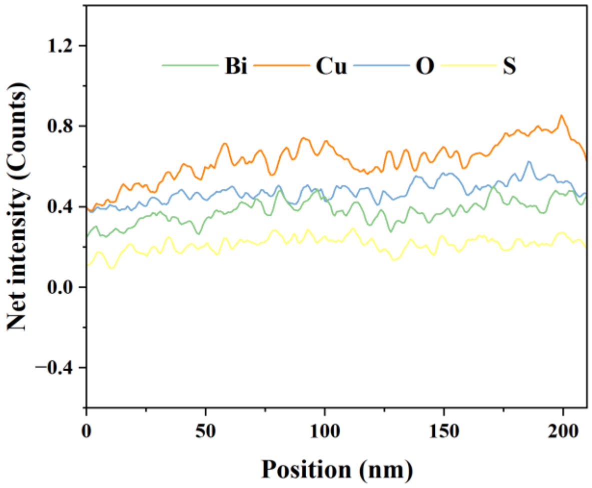

Figure S26 STEM-EDS line-scan profiles of Bi, Cu, O, and S across a representative BiCuOS nanosheet, showing the continuous distribution of all four elements along the scanned region.

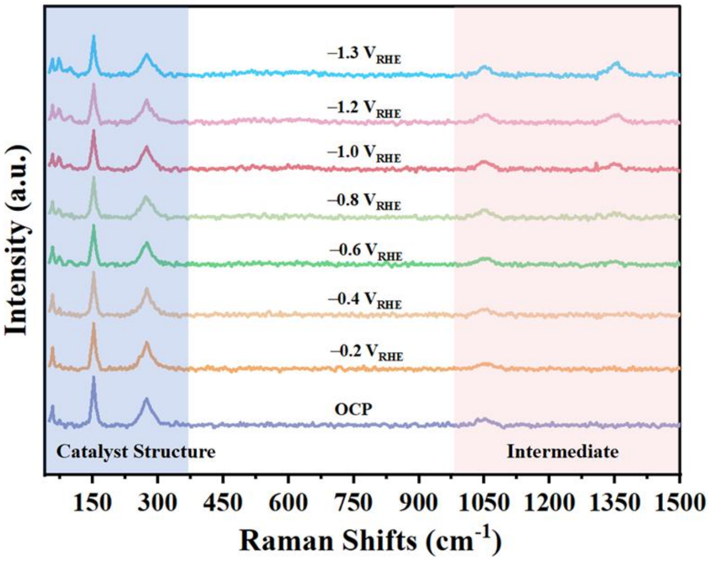

Figure S27 Potential-dependent *in situ* SERS of BiCuOS catalysts in 0.5 M $KHCO_3$ solution under CO_2 bubbling.

Figure S28 Photo of *in-situ* SERS measurement device.

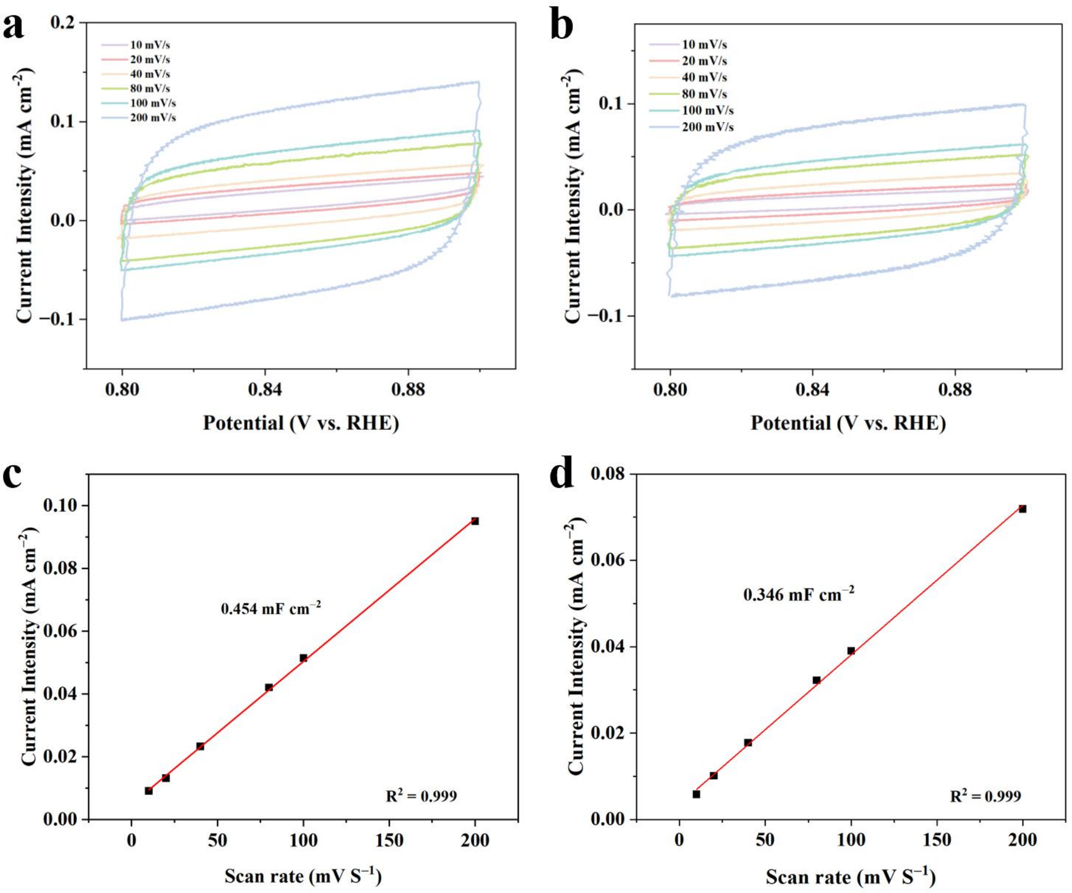

Figure S29 CV curves collected at different scan rates for ECSA measurements in CO_2−saturated 0.5 M $KHCO_3$ solution of Bi_2O_3 **(a)** before and **(b)** after eCO_2R. Difference of charging current at 0.85 V vs. RHE for Bi_2O_3 (c) before and (d) after catalysis against scan rate for determining C_{dl}.

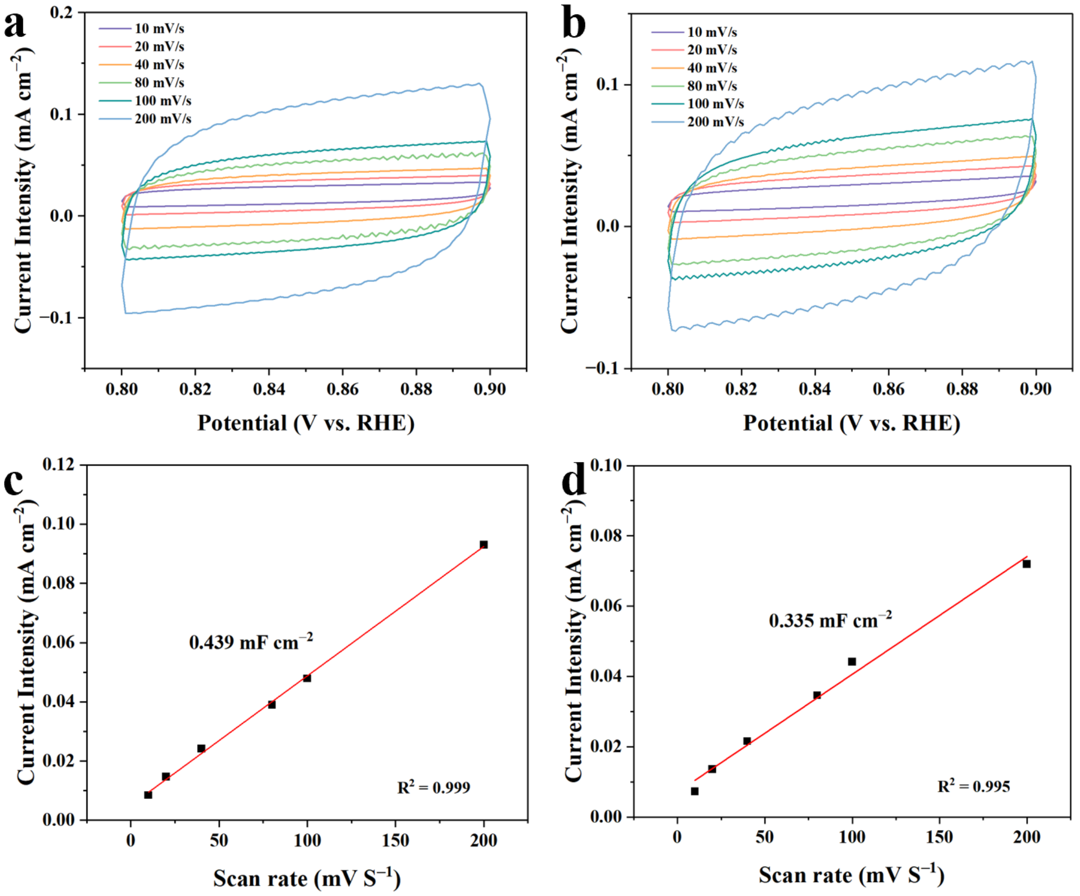

Figure S30 CV curves collected at different scan rates for ECSA measurements in CO_2−saturated 0.5 M $KHCO_3$ solution of Bi_2S_3 **(a)** before and **(b)** after eCO_2R. Difference of charging current at 0.85 V vs. RHE for Bi_2S_3 (c) before and (d) after catalysis against scan rate for determining C_{dl}.

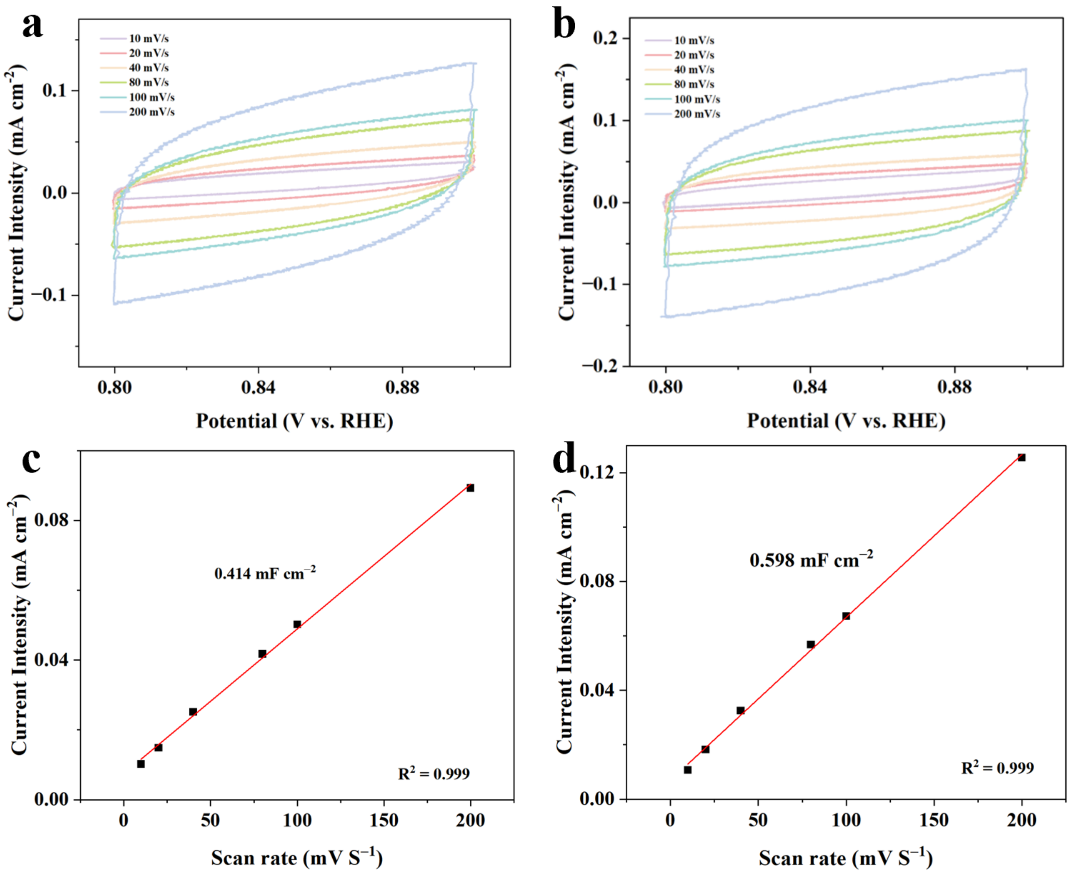

Figure S31 CV curves collected at different scan rates for ECSA measurements in CO_2−saturated 0.5 M $KHCO_3$ solution of BiCuOS **(a)** before and **(b)** after eCO_2R. Difference of charging current at 0.85 V vs. RHE for BiCuOS (c) before and (d) after catalysis against scan rate for determining double−layer capacitance (C_{dl}).

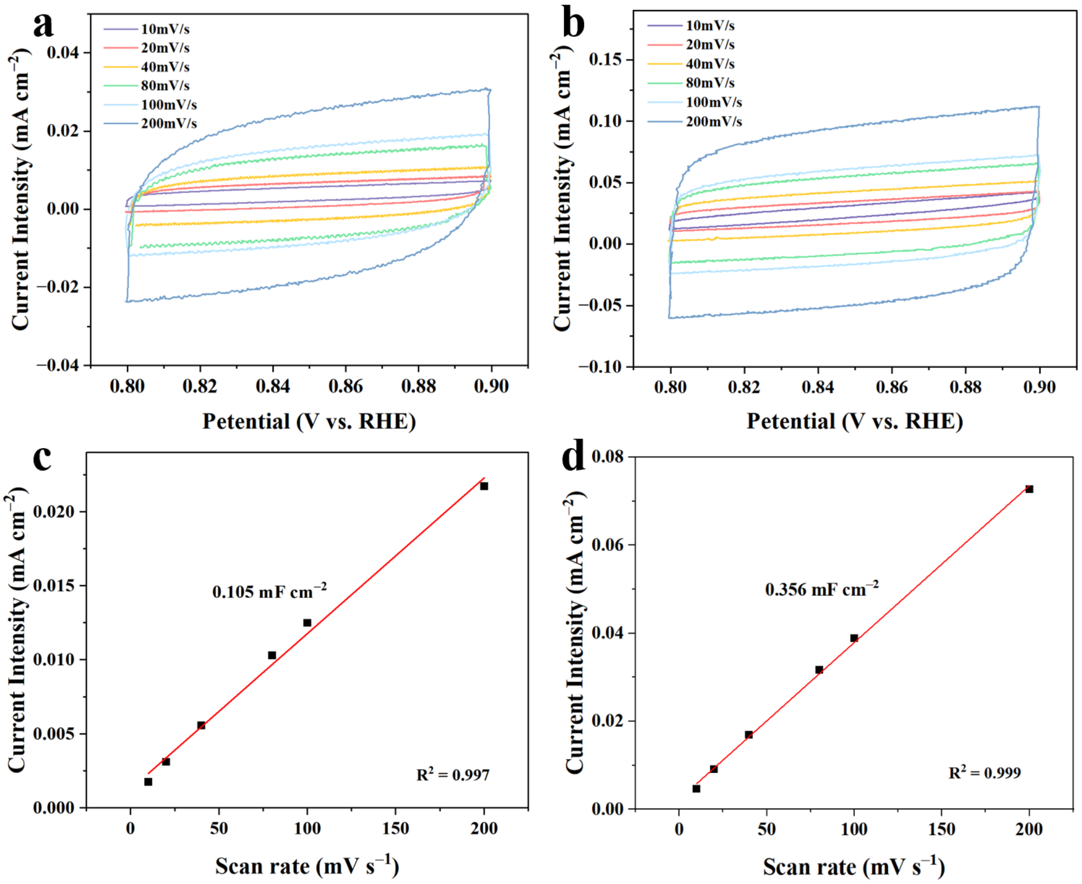

Figure S32 CV curves collected at different scan rates for ECSA measurements in CO_2−saturated 0.5 M $KHCO_3$ solution of Bi_2O_3-Bi_2S_3-Cu_2S heterojunction **(a)** before and **(b)** after eCO_2R. Difference of charging current at 0.85 V vs. RHE for heterojunction sample **(c)** before and **(d)** after catalysis against scan rate for determining double−layer capacitance (C_{dl}).

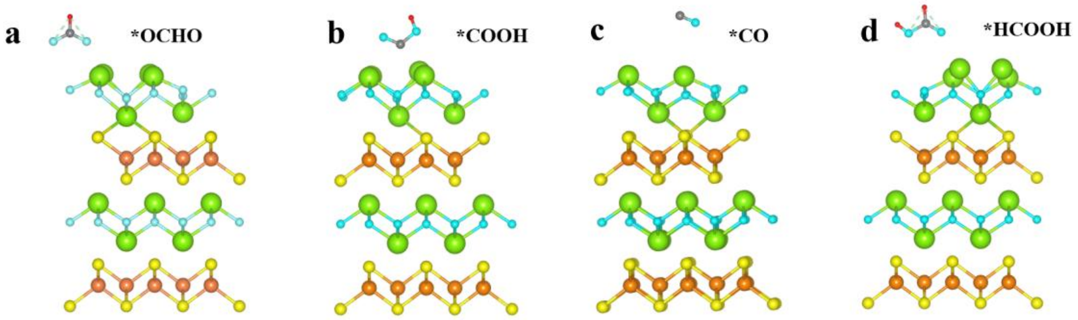

Figure S33 The optimized structures with adsorbed (**a**) *OCHO, (**b**) *CO, (**c**) *COOH, and (**d**) *HCOOH on BiCuOS.

Supplemental Tables

Table S1: Some reported oxidation state Bi-based electrocatalysts for eCO$_2$R to formate in neutral electrolyte.

	electrolyte	**cell type**	**FE Formate**	**stability (h)**	**stability current density (mA cm^{-2})**	
Bi2O3 fractals	0.5 M KHCO$_3$	H-type	87%	26	20	Adv. Funct. Mater.2020, 30, 1906478
Bi2O3 sphere	0.5 M KHCO$_3$	H-type	90%	24	8	ACS Catal. 2020, 10, 1, 743-750
Bi2O3NPs@C	0.5 M KHCO$_3$	GDE	93%	1	150	Angew. Chem. Int. Ed. 2020, 59, 10807-10813
BiPO4NSs	0.5 M KHCO$_3$	H-type	92%	15	8	Angew. Chem. Int. Ed. 2021, 60, 7681-7685
BiCuOSe	0.5 M KHCO$_3$	GDE	93.40%	10	21	Nat Commun 13, 2039 (2022)
Bi2O3NSs@MCCM	0.1 M KHCO$_3$	H-type	93.80%	12	6	Angew. Chem. Int. Ed. 2019, 58, 13828-13833
Bi2O3/BiO2	0.5 M KHCO$_3$	MEA	98.12%	30	220	Nano Lett. 2022, 22, 4, 1656–1664
Bismuth oxide-NGQDs	0.5 M KHCO$_3$	H-type	92.00%	15	29.3	Angew. Chem. Int. Ed. 2018, 57, 12790–12794
Morphology-controlled Bi2O3 nanoparticles	0.5 M NaHCO$_3$	H-type cell	91.00%	23	22	ChemElectroChem 2018, 5, 3741–3747
BiCuOS	**0.5 M KHCO3** **1 M KOH**	**GDE**	**96.60%** **95.70%**	**75** **107**	**50** **100**	**This Work**

Table S2: Relative sensitivity factor (RSF)-corrected XPS surface atomic fractions of BiCuOS before and after eCO$_2$R without oxygen.

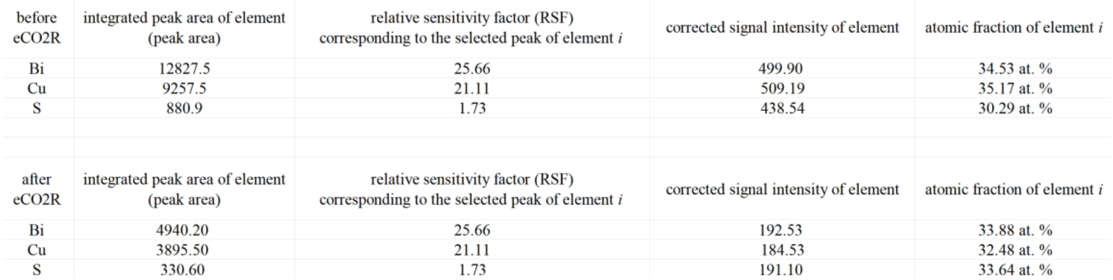

before eCO2R	integrated peak area of element (peak area)	relative sensitivity factor (RSF) corresponding to the selected peak of element *i*	corrected signal intensity of element	atomic fraction of element *i*
Bi	12827.5	25.66	499.90	34.53 at. %
Cu	9257.5	21.11	509.19	35.17 at. %
S	880.9	1.73	438.54	30.29 at. %

after eCO2R	integrated peak area of element (peak area)	relative sensitivity factor (RSF) corresponding to the selected peak of element *i*	corrected signal intensity of element	atomic fraction of element *i*
Bi	4940.20	25.66	192.53	33.88 at. %
Cu	3895.50	21.11	184.53	32.48 at. %
S	330.60	1.73	191.10	33.64 at. %

In XPS quantification, the corrected signal intensity of element *i* is usually written as:

$$I_i^{\mathrm{corr}} = \frac{A_i}{S_i}$$

where:

A_i: integrated peak area of element *i* (peak area)

S_i: sensitivity factor (RSF) corresponding to the selected peak of element *i*

Then, the surface atomic percentage can be expressed as:

$$C_i = \frac{A_i/S_i}{\sum_j A_j/S_j}$$

where:

C_i: atomic fraction of element *i*

the denominator represents the sum of the corrected peak areas of all elements included in the quantification

Table S3: ICP-OES results for the post-electrolysis electrolyte collected after eCO_2R

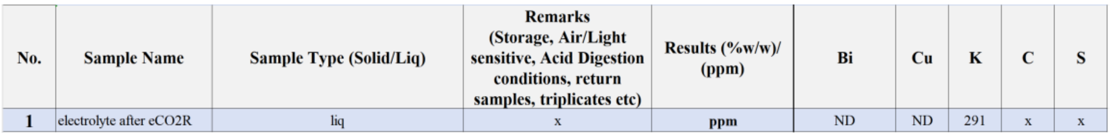

No.	Sample Name	Sample Type (Solid/Liq)	Remarks (Storage, Air/Light sensitive, Acid Digestion conditions, return samples, triplicates etc)	Results (%w/w)/ (ppm)	Bi	Cu	K	C	S
1	electrolyte after eCO2R	liq	x	**ppm**	ND	ND	291	x	x

ICP-OES analysis of the post-electrolysis electrolyte shows that both Bi and Cu are below the detection limit, indicating negligible metal leaching during eCO_2R.